HAL
open science

Measurement of kinematic fields via DIC for impact engineering applications

François Hild, Amine Bouterf, Stéphane Roux

To cite this version:

François Hild, Amine Bouterf, Stéphane Roux. Measurement of kinematic fields via DIC for impact engineering applications. International Journal of Impact Engineering, 2019, 130, pp.163-171. 10.1016/j.ijimpeng.2019.04.007 . hal-02096299

HAL Id: hal-02096299

https://hal.science/hal-02096299

Submitted on 11 Apr 2019

HAL is a multi-disciplinary open access archive for the deposit and dissemination of scientific research documents, whether they are published or not. The documents may come from teaching and research institutions in France or abroad, or from public or private research centers.

L'archive ouverte pluridisciplinaire **HAL**, est destinée au dépôt et à la diffusion de documents scientifiques de niveau recherche, publiés ou non, émanant des établissements d'enseignement et de recherche français ou étrangers, des laboratoires publics ou privés.

Measurement of kinematic fields via DIC for impact engineering applications

François Hild,[a,b] Amine Bouterf,[a] Stéphane Roux[a]

(a): Laboratoire de Mécanique et Technologie (LMT)

ENS Cachan / CNRS / Paris-Saclay University

61 avenue du Président Wilson, 94235 Cachan Cedex, France

(b): corresponding author.

Abstract

Two dynamic Brazilian tests are analyzed via digital image correlation for acquisition rates equal to 5 and 10 million frames per second. Displacements of the order of 1 mm, velocities of the order of ± 250 m/s, and accelerations as high as $\pm 4 \times 10^7$ m/s^2 are measured with spacetime DIC. Uncertainty quantifications enable spacetime DIC to be compared with instantaneous analyses. The gains provided by the temporal regularization are very significant for the acceleration fields. The observed levels are consistent with a priori estimates.

Key words: Digital Image Correlation, Full-field measurements, Spatial registration, Temporal registration, uncertainty quantification.

Email addresses: `francois.hild@ens-paris-saclay.fr` (François Hild,[a,b]), `amine.bouterf@ens-paris-saclay.fr` (Amine Bouterf,[a]), `stephane.roux@ens-paris-saclay.fr` (Stéphane Roux[a]).

1 Introduction

In impact engineering, as in other areas of solid mechanics, the understanding and quantification of the loading conditions is one key point to be addressed. One of the most used loading devices to characterize the material behavior at high-rate loadings is split Hopkinson pressure bars [1,2]. For many years the analysis of such tests relied on the use of strain gauge data and thus requires long bars to be used. These strain data then enabled the loading conditions to be inferred on the interfaces between the bars and the studied sample. This situation may eventually change with the use of full-field measurements that enable the experimentalist to focus more on the sample itself.

Among various optical techniques, Digital image correlation (DIC) and its 3D extension for measuring 3D deformations via stereocorrelation [3] is gradually emerging as suitable and reliable for high rate deformation and shock studies [4,5]. DIC, which was introduced in the early 1980s [6,7], was very quickly applied to the study of cracking under dynamic loading. As early as 1985, a first series of results was reported for a 3-point flexural test on Araldite B samples [8]. The authors used a Cranz-Shardin camera, measured displacement fields and compared them to the static solution for the estimation of stress intensity factors. A good agreement was found when these results were compared with those given by the analysis of caustics. This type of analysis was continued with improved experimental conditions as well as post-processing procedures [9].

With the advent of digital high speed cameras [10], the number of studies have broadened and are no longer exclusively devoted to defense applications (*e.g.,* see Refs. [11–19]). In the International Journal of Impact Engineering,

the first (and as of today [20], the most cited) paper on image correlation was published by Tiwary et al. [21]. Displacement, velocity, acceleration, strain and strain rate fields were reported. All of them were based on instantaneous stereocorrelations with a commercial code. The measured displacement fields were subsequently processed in order to compute all differentiated fields. The subsequent publications [22–26] reported only strain fields, which is a standard output of instantaneous DIC codes. In the following papers [27–29], the displacement fields were always reported, and sometimes the strain and velocity fields. The uncertainty were evaluated by Besnard et al. [30] for deformed shape measurements and strain rates. Strain fields were then the primary kinematic data that were discussed in the following publications [31–34].

The year 2014 saw no papers using DIC being published in the Journal (Figure 1). Over the previous five years a total of 14 papers was published. Over the next four years (2018 included), a total of 39 papers was published. Of those, only a few [35–41] did not only report displacement and/or strain fields, which required additional processing when instantaneous analyses were performed. It is worth noting that uncertainty quantifications were not reported for any of the last 39 papers.

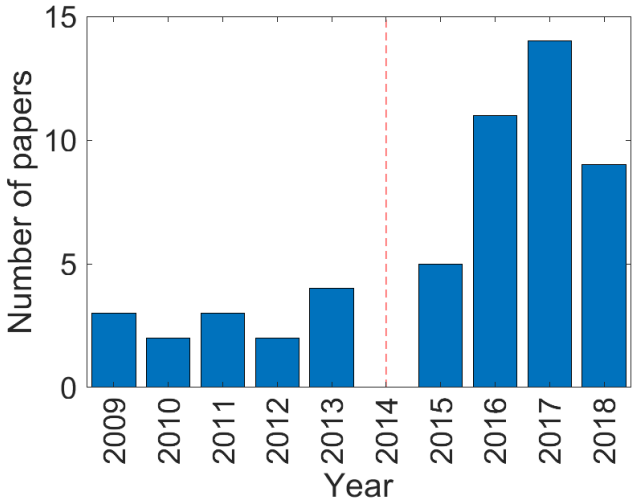

Fig. 1. Number of papers dealing with DIC and published yearly in the International Journal of Impact Engineering [20]

From this short literature review, it is concluded that virtually all studies used existing (and mostly commercial) DIC codes. It follows that most of the reported kinematic fields were those directly provided by the latter ones (*i.e.,* displacement and strain fields). Further, all reported DIC analyses were based on *instantaneous* registration, namely, the registration of image(s) of one single deformed configuration with respect to the reference configuration. As already mentioned, when the analyses required strain rate, velocity or acceleration fields, additional post-processing had to be performed [21,30,35–41].

An alternative route to instantaneous analyses is to perform local time interpolations in order to measure directly strain rate fields [42]. Global spatiotemporal analyses were also introduced [43,44] in which displacement and velocity fields were a priori interpolated along the time axis in the registration procedure, not a posteriori as would be performed with instantaneous DIC. Such techniques were applied to videos acquired with a camcorder [43] or high speed cameras [44]. Because the reference image played a central role in such

analyses, the gain in displacement uncertainty was not shown to be as high as expected with noiseless references [44]. A denoising procedure was introduced very recently to address this particular point [45].

In the following, instantaneous and spacetime DIC analyses will be compared. Two dynamic Brazilian tests performed in split Hopkinson pressure bars and monitored with an ultra-high speed camera will be analyzed. The acquisition rate was set to 5 and 10 million frames per second. Five different kinematic fields will be reported namely, displacement, velocity and acceleration fields on the one hand. From these fields, the mean crack opening displacement, velocity and accelerations will be discussed. On the other hand, strain and strain rate fields will also be studied. In order to understand the differences between instantaneous and spacetime DIC, the uncertainties on the five kinematic data will be analyzed thanks to the fact that movies with no motions were available for both experiments.

2 Instantaneous and spacetime DIC

Two different approaches will be compared herein, namely, instantaneous and spacetime DIC. The first one consists in registering pairs of images whereas the second one performs the registration over whole videos (*i.e.,* series of pictures).

2.1 Instantaneous DIC

In the following, a global approach will be used for the spatial registration. The displacement field $\boldsymbol{u}(\boldsymbol{x}, t)$ is discretized by using finite element shape

functions [46] $\boldsymbol{\varphi}_i(\boldsymbol{x})$

$$\boldsymbol{u}(\boldsymbol{x},t) = \upsilon_i(t)\boldsymbol{\varphi}_i(\boldsymbol{x}) \tag{1}$$

where $\upsilon_i(t)$ are the nodal displacements to be determined by minimizing the global residuals over the considered region of interest (ROI)

$$R(t) = \sum_{ROI} \rho^2(\boldsymbol{x},t) \tag{2}$$

with respect to the unknown amplitudes $\upsilon_i(t)$, which are gathered the column vector $\{\boldsymbol{\upsilon}(t)\}$, where

$$\rho(\boldsymbol{x},t) = f(\boldsymbol{x},t) - f_0(\boldsymbol{x}) \tag{3}$$

denotes the gray level residual computed for any pixel $\boldsymbol{x}$ of the ROI, $f(\boldsymbol{x},t)$ the gray level picture of the current configuration (at time t), and $f_0(\boldsymbol{x})$ the reference picture.

A priori estimates of the displacement and strain uncertainties for instantaneous analyses have been proposed [47]. Since the outputs of DIC analyses are displacement *fields*, the covariance matrix of the measured degrees of freedom has to be evaluated for characterizing measurement uncertainties [48]. In global approaches, each degree of freedom is not determined independently of the other ones. Consequently, they are correlated (in a statistical sense) and the covariance matrix is required to fully characterize their variances *and* covariances. For local (*i.e.,* subset-based) approaches, as soon as interrogation windows overlap, the displacement measurements are no longer independent (*i.e.,* some correlations exist since part of the pixels are shared by neighboring windows). It was shown that the covariance matrix $[\boldsymbol{C}_\upsilon]$ of the measured degrees of freedom $\{\boldsymbol{\upsilon}(t)\}$ is related to the Hessian at convergence of the minimization scheme $[\boldsymbol{M}]$

$$[\boldsymbol{C}_{\boldsymbol{\upsilon}}] = 2\sigma_f^2[\boldsymbol{M}]^{-1} \tag{4}$$

where σ_f^2 is the variance of acquisition noise.

When a time series of pictures is analyzed, instantaneous DIC is usually run [3]. For each new image, the initial displacement estimate is that of the converged solution of the previous image pair. In the following analyses, three-noded finite elements will be considered (*i.e.,* linear displacement interpolations within each triangular element). Further, the reference image will not be the first image of the time series but will be denoised [45,49]. Once the nodal displacements are determined, the strain fields are evaluated by exact differentiation of the spatial shape functions. The nodal velocities are determined by forward finite differences of the nodal displacements, and the nodal accelerations by forward finite differences of the nodal velocities. The strain rates are obtained by using the nodal velocities and the exact derivatives of the shape functions.

2.2 Spatiotemporal DIC

An alternative route to the previous approach is to consider global analyses in time [43–45,49]. Instead of performing a series of instantaneous minimizations of instantaneous residuals, a *single* spatiotemporal minimization is run, and the following gray level residual

$$\mathcal{R} = \sum_t R(t) \tag{5}$$

is minimized with respect to the kinematic parameters. Different parameterizations of the displacement fields have been discussed [44]. In the following, space/time separations are assumed

$$\boldsymbol{u}(\boldsymbol{x}, t) = \upsilon_{ij} \boldsymbol{\varphi}_i(\boldsymbol{x}) \phi_j(t) \tag{6}$$

where υ_{ij} denote the spatiotemporal unknowns to be determined. In the present study finite element discretizations will also be used for the temporal shape functions $\phi_j(t)$. The modal decomposition introduced in Ref. [45], which enables instantaneous DIC codes to be extended to spacetime analyses in an non-intrusive way, was implemented.

The a priori uncertainties can also be estimated by extending the previous results to spatiotemporal analyses [44]. It is first based on the spatiotemporal Hessian $[\boldsymbol{N}]$, which is constructed with the spatial Hessian $[\boldsymbol{M}]$, and the temporal matrix $[\boldsymbol{\Phi}]$ such that

$$N_{ijkl} = M_{ik}\Phi_{jl} \tag{7}$$

with

$$\Phi_{ij} = \sum_t \varphi_i(t)\varphi_j(t) \tag{8}$$

It follows that the covariance matrix of spatiotemporal degrees of freedom becomes

$$C(\upsilon_{ij}, \upsilon_{kl}) = \sigma_f^2 \left(\Phi_{jp}^{-1}\Phi_p\Phi_{lq}^{-1}\Phi_q + \Phi_{jl}^{-1}\right) M_{ik}^{-1} \tag{9}$$

with

$$\Phi_k = \sum_t \varphi_k(t) \tag{10}$$

2.3 Reference picture f_0

In the sequel, high speed experiments will be analyzed. With the ultra-high speed camera used herein, a full video will be acquired prior to the experiment per se. Consequently, there exists a set of images with no motions. This series of images is averaged time-wise for each pixel to form a denoised reference picture f_0. There is no need to follow the denoising procedure proposed in

Refs. [45,49].

When considering a denoised reference image, the factor 2 in Equation (4) no longer appears. The direct consequence is that the standard displacement uncertainties are divided by a factor of 2 for instantaneous analyses. Further, the first term in Equation (9) vanishes for denoised reference pictures [44]. Consequently, the covariance matrix $C(\upsilon_{ij}, \upsilon_{kl})$ is equal to $\sigma_f^2 \Phi_{jl}^{-1} M_{ik}^{-1}$. It follows that the displacement uncertainties will be inversely proportional to the square root number of pictures when linear interpolations are used.

3 Uncertainty quantifications

Before reporting any measurement, it is important to evaluate the corresponding uncertainties [50]. This type of analysis was carried out on time series for which no motion occurred.

3.1 Dynamic Brazilian tests

Brazilian tests enable the tensile strength of brittle materials such as concrete and rocks to be assessed [51,52]. They consist in performing compression tests on disks or cylinders. In each reported test, a 72 mm in diameter and 10 mm thick disk made of Ductal® concrete was loaded up to failure under impact. The dynamic tests were carried out via Hopkinson bars [2] made of aluminum alloy. The loading system consisted of a pressurized air gun, a 60 mm in diameter and 80 mm long projectile, an input bar with the same diameter and a length of 4.5 m, and an output bar with a length of 2 m. The speed of the input bar was equal to about 6 m/s. In both tests, the observed sample

surface was speckled by random spraying of black and white paints.

One spot light (Dedolight®, maximum power: 400 W) and two light heads (Dedocool®, maximum power: 250 W) were switched on just before starting the tests to avoid heating. Such lighting power was needed because of the very high acquisition rates used herein. It enabled for enhanced contrast in the acquired videos, which allows the measurement uncertainties to be lowered [47]. A Shimadzu® HPV-X ultra-high speed camera was used to record the deformation of the specimen surface during the tests. Image videos with definition of 400 $\times$ 250 pixels were acquired. The lens used with the camera was a 50 mm Nikon® F-Mount. The physical size of one pixel was set to 360 µm, which maximized the number of pixels of the monitored sample surfaces.

3.2 5 Mfps video

First, an acquisition rate of 5 million frames per second (fps) was selected. The (fixed) exposure time was equal to 110 ns. A video of 256 images was recorded. The reference image was then constructed as the temporal average for any pixel $\boldsymbol{x}$. From this picture, the root mean square (RMS) difference was computed for each time. This quantity evaluates the noise level of the camera. Figure 2 shows the change of the RMS difference. The average level is equal to 147 gray levels, which is 0.2 % of the dynamic range (*i.e.,* 65500 gray levels). This level is extremely low in comparison with high speed or even low speed cameras [5].

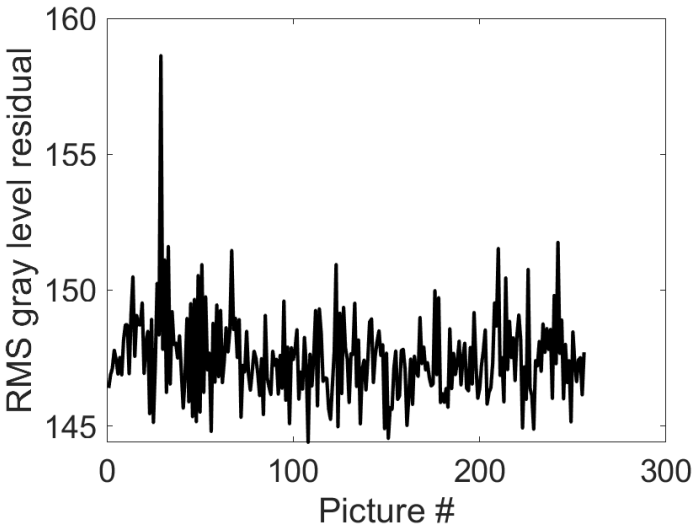

Fig. 2. RMS gray level difference between the acquired pictures and their temporal average for the 5 Mfps experiment

Instantaneous and spatiotemporal analyses were then run with this set of pictures. A finite element mesh was adapted to the actual sample geometry (Figure 3). The mean element edge was equal to 3 pixels (or 1.1 mm). In order to filter out spatial fluctuations of displacement fields, a regularization length equal to 10 pixels was selected [53]. For spatiotemporal analyses, linear interpolations are considered along the temporal axis. Because of acquisition noise, each nodal displacement is a random variable with variances and covariances. For the sake of simplicity, the temporal fluctuations of measured nodal displacements are only characterized by the corresponding standard deviation in time. The measurement uncertainty is then *defined* in the following analyses as the spatial average of all standard deviations.

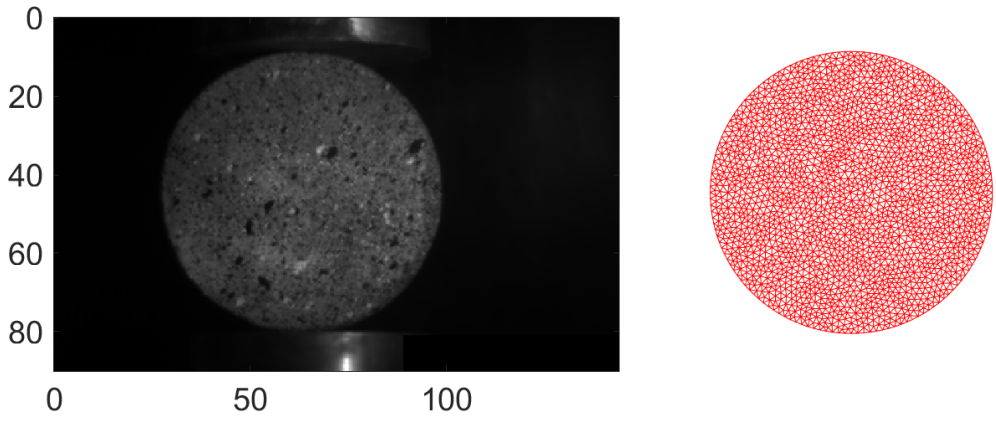

(a) (b)

Fig. 3. (a) Denoised reference image. (b) Corresponding mesh made of 3-pixel elements for the 5 Mfps experiment. The dimensions are expressed in mm

In Figure 4, the measurement uncertainties are reported for displacements, velocities, principal strains and their rates. All these quantities are plotted as functions of the time interval over which the DIC analyses are performed. The lower level (*i.e.,* 0.2 µs) corresponds to instantaneous DIC. For all the reported quantities, the larger the time interval of the interpolation, the lower the uncertainties. This trend is to be expected since it corresponds to stronger temporal regularization. When the reference picture is denoised, it is anticipated that the standard displacement uncertainty σ_u is inversely proportional to the square root of the number of pictures per interval [44], or equivalently to the time interval ℓ_t. This trend is depicted by the green dashed line in Figure 4(a) as the best log-fit. This assumption is not totally satisfied. It can be understood by noting that there are correlated temporal fluctuations in acquisition noise (see Figure 2). The blue dashed line correspond to the a priori estimates constructed with the Hessian of instantaneous DIC. The diagonal

terms correspond to the variances of each measured nodal displacement. Its average is then computed, from which the a priori estimate corresponds to its square root, namely, the a priori standard displacement uncertainty. In the present case, the a priori estimate virtually coincides with the log-fit.

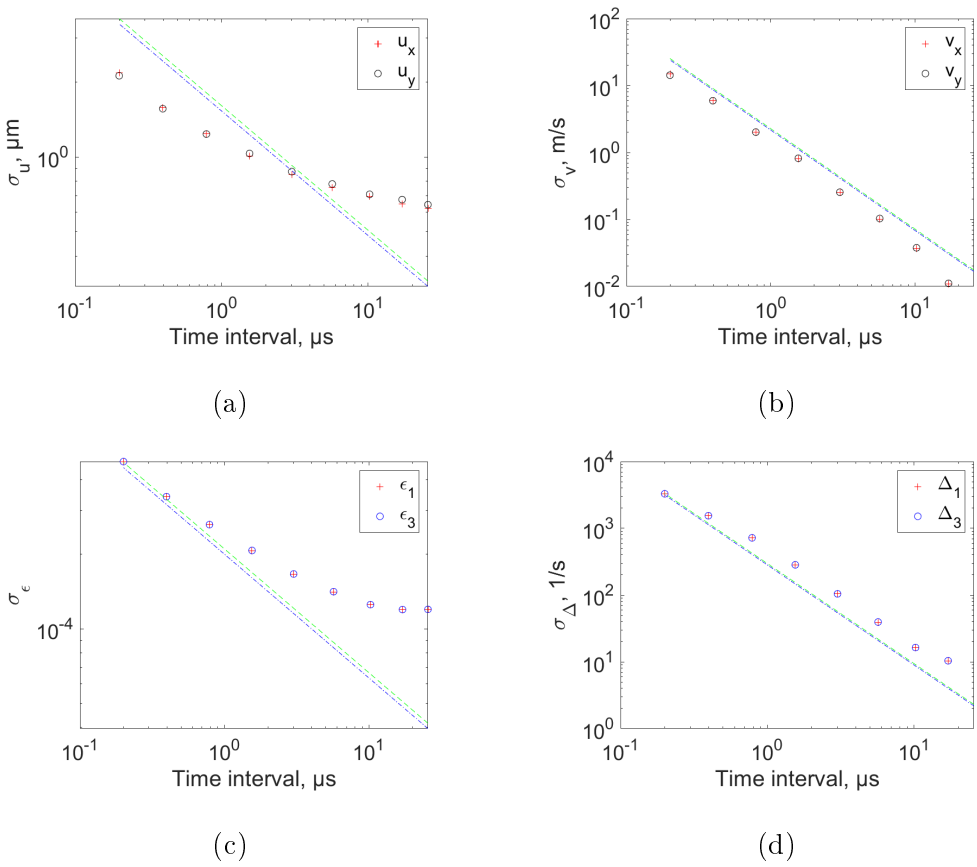

Fig. 4. Standard displacement (a), velocity (b), strain (c) and strain rate (d) uncertainties as functions of the time interval ℓ_t for the 5 Mfps experiment

The velocity uncertainty σ_v is equal to $\sqrt{2}\sigma_u/\ell_t$. From the previous analysis, this leads to the green dashed line shown in Figure 4(b), which slightly overestimates the actual levels. However, the general trend is very well captured. This is also true for the a priori estimate (blue dashed line). The strain uncertainty, which depends on the displacement interpolation [47], is proportional to the displacement uncertainty divided by the regularization length ℓ_r [53]. As

for the displacements, this interpolation underestimates the standard strain uncertainties (for the same reasons, see Figure 4(c)). Last, the strain rate uncertainty σ_Δ is equal to $\sqrt{2}\sigma_\epsilon/\ell_t$, which is depicted by the green dashed line in Figure 4(d). Again a very good agreement is observed. The same observations apply for the a priori estimates.

Since acceleration fields will be sought, linear shape functions were not sufficient. Six cubic B-splines were selected instead to model the displacement fields for the first 150 pictures of the video. With the chosen parameterization (see below), there were 6 degrees of freedom to be compared with 150 for instantaneous DIC. Consequently, it is expected that the measurement uncertainties will be lower for spacetime DIC when compared with instantaneous analyses (Table 1). The gain in uncertainty is rather small (*i.e.,* ≈ 4 on average) for displacements and strains, becomes more important (*i.e.,* $\approx 4^3$) for velocities and strain rates, and very significant for accelerations (*i.e.,* $\approx 4^5$). For the latter, the cubic interpolation and the continuity of the accelerations yield very significant gains (*i.e.,* three orders of magnitude).

Table 1

Standard uncertainties for instantaneous DIC (*i.e.,* $\ell_t = 0.1$ µs) and spline interpolation with six degrees of freedom

Standard uncertainty	instantaneous DIC	spatiotemporal DIC	ratio
σ_u (µm)	2.1	0.6	3.5
σ_v (m/s)	15	0.2	65
σ_a (m/s^2)	1.3×10^8	1.1×10^5	1200
σ_ϵ	4.7×10^{-4}	1.3×10^{-4}	3.7
σ_Δ (1/s)	3.3×10^3	36	91

The results of Table 1 show that significant gains in terms of measurement uncertainties can be achieved thanks to spatiotemporal analyses. This is particularly true for acceleration fields (*i.e.,* three orders of magnitude in the present case), and to a lesser degree for velocity and strain rate fields (*i.e.,* two orders of magnitude). Such performances are made possible thanks to higher order interpolations in the time domain.

3.3 10 Mfps series

The second series was a sequence of 128 frames, which were acquired at a rate of 10 million fps. The (fixed) exposure time was equal to 50 ns. Once the reference picture was constructed, the noise level of the camera was estimated. Figure 5 shows the change of the RMS difference with time. The average level is equal to 192 gray levels, which is 0.3 % of the dynamic range. Even though higher than in the previous case, this level is very low given the very high

acquisition rate. As for the previous case, the temporal fluctuations are not totally uncorrelated.

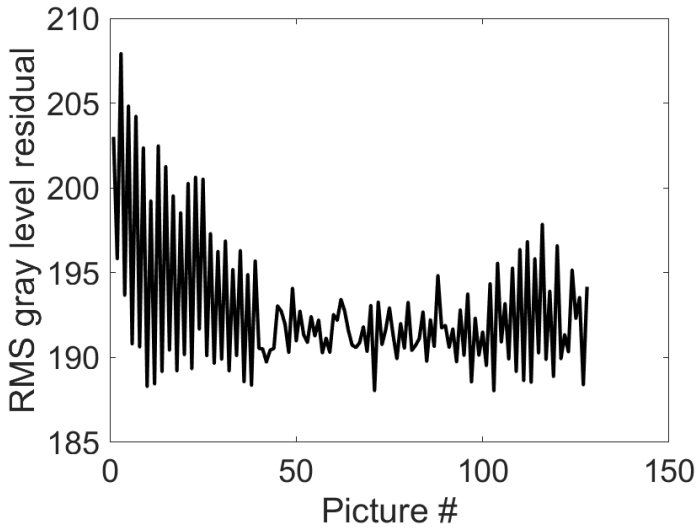

Fig. 5. RMS gray level difference between the acquired pictures and their temporal average for the 10 Mfps experiment

A finite element mesh (average element edge equal to 3 pixels or 1 mm) was also adapted to the actual sample geometry (Figure 6). For spatiotemporal analyses, only linear interpolations were considered along the temporal axis (since no acceleration fields will be analyzed hereafter).

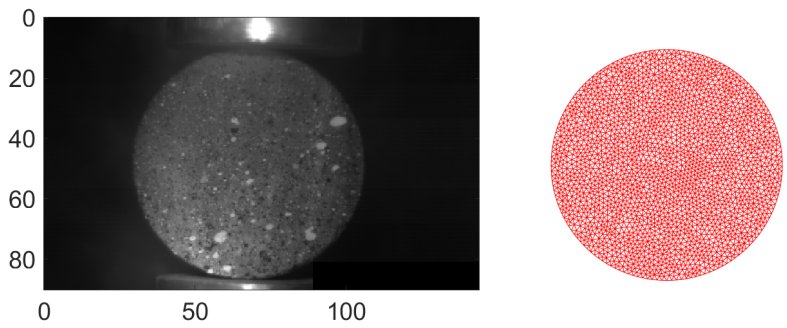

(a) (b)

Fig. 6. (a) Denoised reference image. (b) Corresponding mesh made of 3-pixel elements for the 10 Mfps experiment. The dimensions are expressed in mm

For comparison purposes with the previous results, the measurement uncertainties are reported for linear interpolations in Figure 7. When compared to Figure 4 the overall levels are higher. This is to be expected since the acquisition rate is higher and the associated noise level as well [5]. The displacement and strain uncertainties also decrease with ℓ_t but not with a $-1/2$ slope in a log-log plot. Conversely, the velocity and strain rate uncertainties have a variation with ℓ_t described by a power law of exponent $-3/2$. These new results are consistent with those reported for the 5 Mfps video.[1]

[1] The acquisitions at 5 and 10 Mfps show temporal fluctuations (Figures 2 and 5) that explain the deviations observed in Figures 4(a,c) and 7(a,c) with respect to the expected trends. It is worth noting that these effects are less pronounced when temporal derivatives are applied (see Figures 4(b,d) and 7(b,d)).

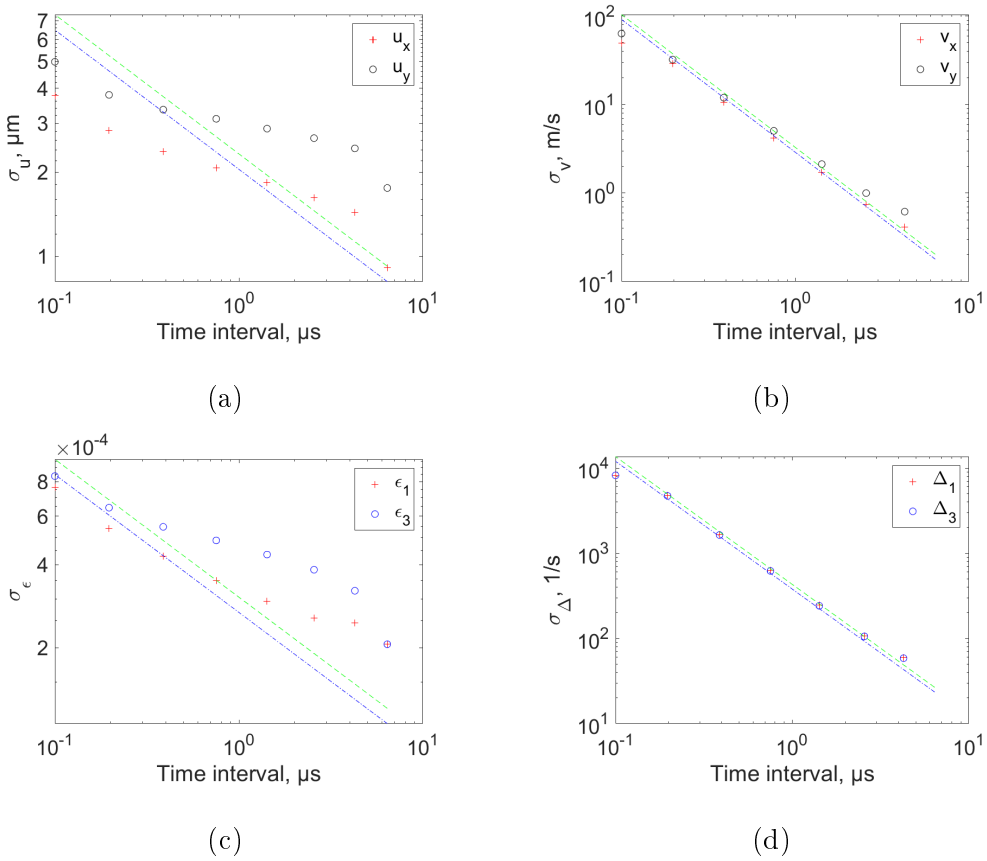

Fig. 7. Standard displacement (a), velocity (b), strain (c) and strain rate (d) uncertainties as functions of the time interval ℓ_t for the 10 Mfps experiment

All these uncertainty quantifications showed that the levels of the investigated kinematic variables can be made very small even though the acquisition rate was very high. All the general trends to be expected by time regularization were observed. Last, the a priori estimates were very close to the power law fits of the raw uncertainties. When comparing the uncertainties corresponding to the two acquisition rates, the difference in level is directly related to acquisition noise (Figures 2 and 5), namely, the higher the acquisition rate, the higher the noise level, and the higher the measurement uncertainties. Conversely, for acquisition rates less than 5 Mfps, it was shown that the measurement uncertainties could be further decreased [5].

It is worth remembering that the present uncertainty quantifications were performed with videos that were acquired under the very same conditions of the actual experiment (*i.e.,* surface of interest, optical setup, illumination, acquisition rate) but with a motionless sample. Thus, such quantifications do not account for blur induced by the motions of the sample during the time exposure (*e.g.,* 50 ns for an acquisition rate of 10 Mfps). As will be discussed farther down, the displacement amplitude for a maximum velocity of 20 m/s is about 3×10^{-3} pixel. For the lower acquisition rate, the maximum velocity is higher, 200 m/s, and the exposure time longer, hence the displacement during the acquisition time is of order 0.06 pixel at most. The effect of motion blur is thus expected not to be a limiting factor in the present experiments.

3.4 10 Mfps series

The first analyzed video consisted of 128 frames acquired at a rate of 10 Mfps. The acquisition was started after the specimen had already been fractured (Figure 8). It is therefore expected that most of the kinematics is associated with a free flight condition (*i.e.,* constant velocity).

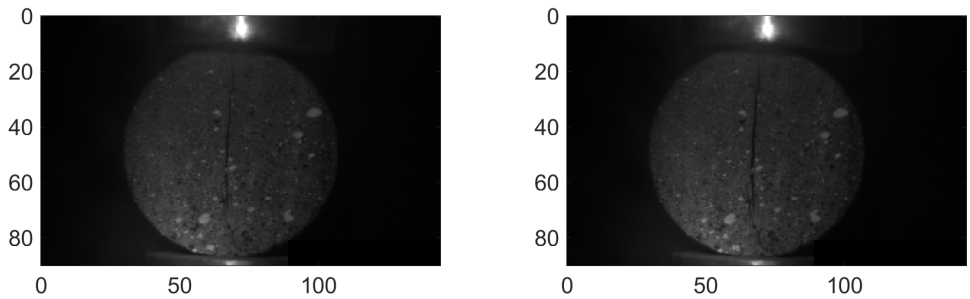

(a) (b)

Fig. 8. (a) Initial and (b) final frame of the 10 Mfps video. The dimensions are expressed in mm

In order to account for the presence of the dominant crack, a node splitting technique was followed to enable displacement discontinuities to occur. The following steps were considered:

- a first instantaneous DIC analysis was run for the first frame of the video, namely, that for which only the dominant crack was present. The initial mesh was considered in which no displacement discontinuity was accounted for (Figure 6)
- From the gray level residual map, the crack path was easily selected (Figure 9) since the crack opening is significant (Figure 8). The advantage of using the residuals instead of the deformed image was that the crack was positioned in the reference frame (consistent with the Lagrangian description used herein).
- The mesh was then adapted to the crack path so that displacement discontinuities were enabled. Given the fact that a node splitting technique was used, the nodal crack opening displacements and velocities could be directly computed as differences of twin nodes.

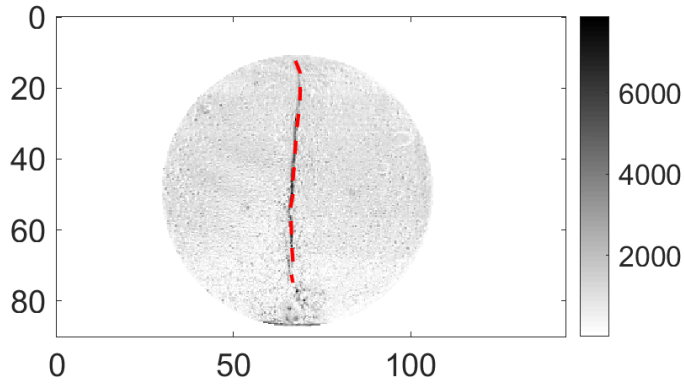

Fig. 9. Absolute gray level residual of the instantaneous registration of the first image of 10 Mfps video. The dashed line corresponds to the selected crack path. The dimensions are expressed in mm

Figure 10 shows displacement fields for the last frame of the video when different temporal discretizations were considered. There is virtually no effect of the discretization for this field. Since one of the DIC calculation was performed with a single (linear) temporal element, it proves that the hypothesis of vanishing accelerations was satisfied (*i.e.,* free flight of fragments). Further, the displacement discontinuity is clearly visible for all displacement fields.

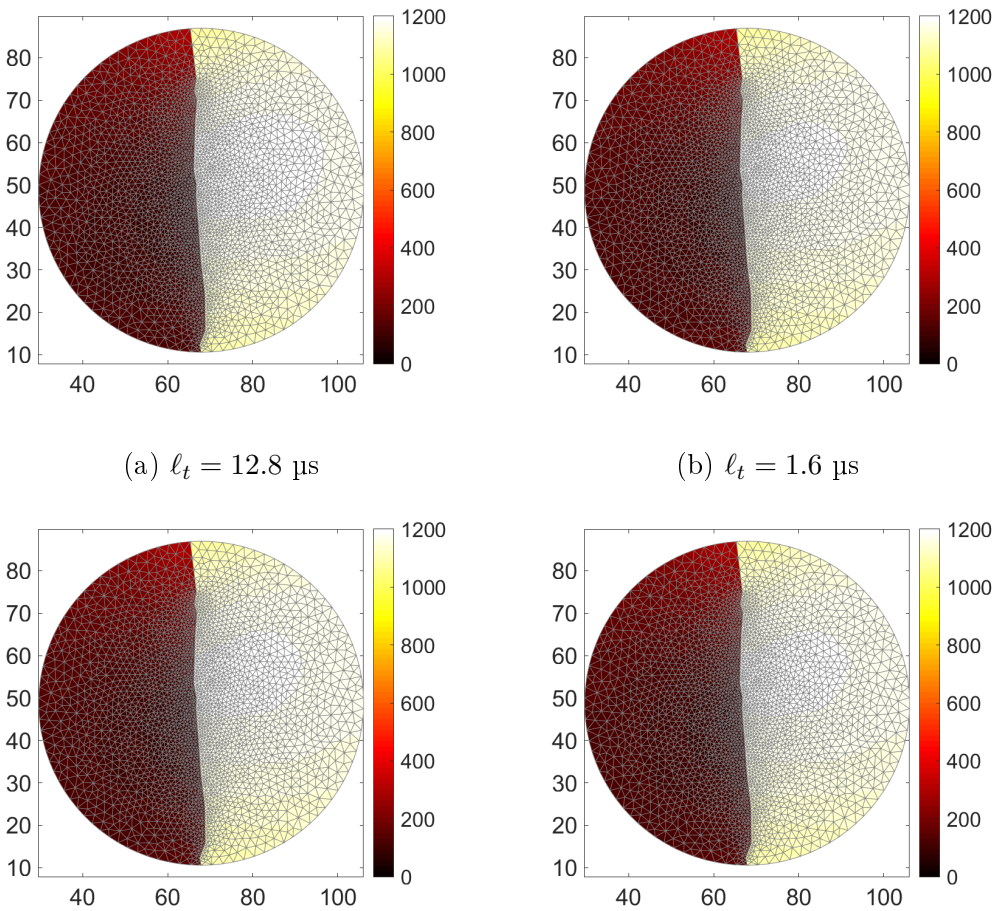

(a) $\ell_t = 12.8$ µs

(b) $\ell_t = 1.6$ µs

(c) $\ell_t = 0.8$ µs

(d) $\ell_t = 0.2$ µs

Fig. 10. Horizontal displacement field (expressed in µm) at the end of the video for different time discretizations

This observation was further confirmed by analyzing the mean RMS residuals reported in Figure 11. The fact that they were independent of the discretization level proves that the use of a single temporal element was sufficient to describe the temporal history of the test. Conversely, their mean level was 4 times higher than that associated with noise, which indicates that the spatial discretization was not fully consistent with the experiment (*i.e.*, only one crack was explicitly accounted for in the present case whereas a more complex crack pattern was taking place).

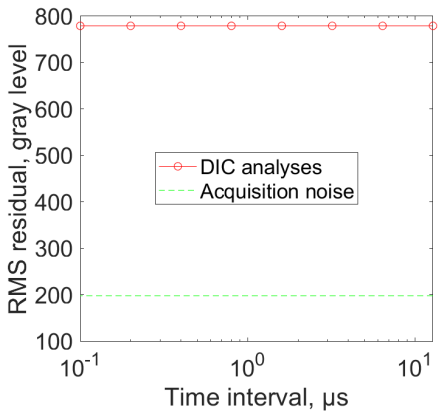

Fig. 11. RMS gray level residual for different time discretizations.

In Figure 12, the horizontal velocity fields are reported for the last frame and for different temporal discretizations. Contrary to the previous case, velocity fluctuations are observed. Their origin can be understood by the fact that rigid body rotations occurred at the very end of the video, which were not fully captured by the spacetime interpolations.

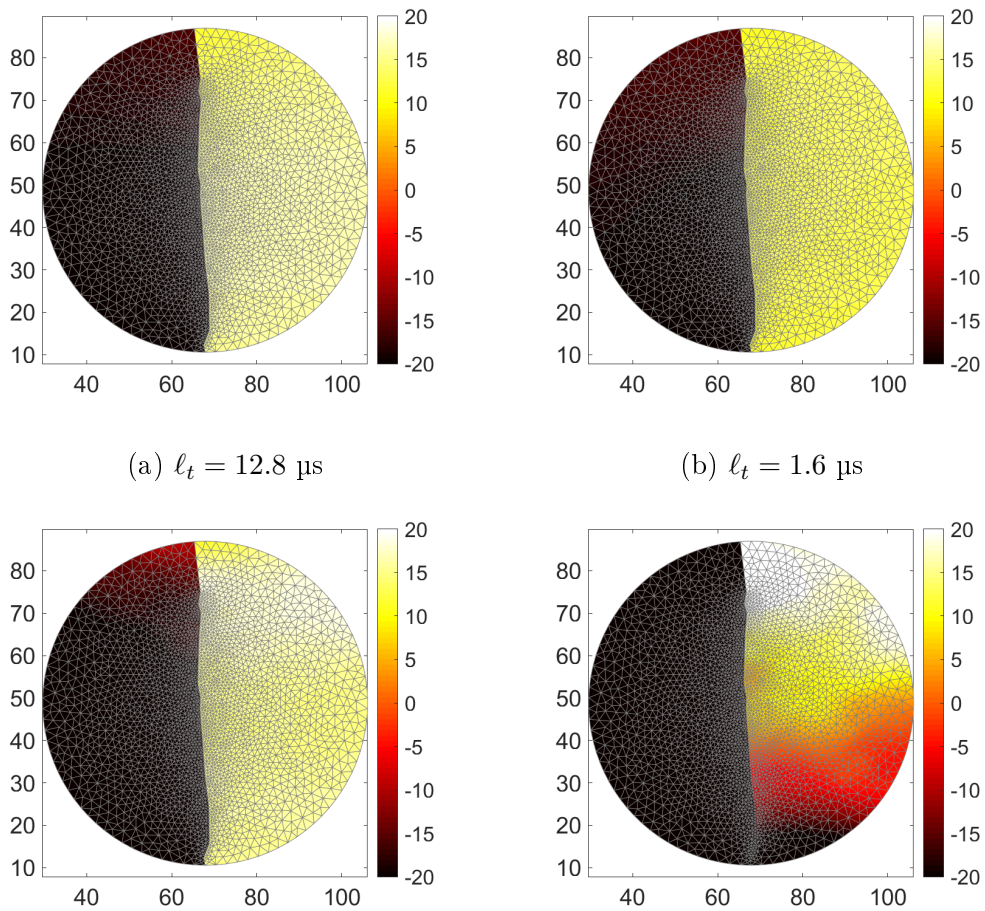

(a) $\ell_t = 12.8$ µs (b) $\ell_t = 1.6$ µs

(c) $\ell_t = 0.8$ µs (d) $\ell_t = 0.2$ µs

Fig. 12. Horizontal velocity field (expressed in m/s) at the end of the video for different time discretizations

From the measured displacement fields and corresponding velocity fields, the crack opening displacement and velocities were obtained as mean averages of the displacements (or velocities) of the two halves of the sample. Figure 13 shows their temporal history for different discretization levels. For the crack opening displacements (Figure 13(a)), the eight temporal discretizations lead to very similar results, which was expected from the gray level residuals (Figure 11). This is no longer the case of the crack opening velocities (Figure 13(b)) for which only the last three discretizations yield consistent results of 37 m/s.

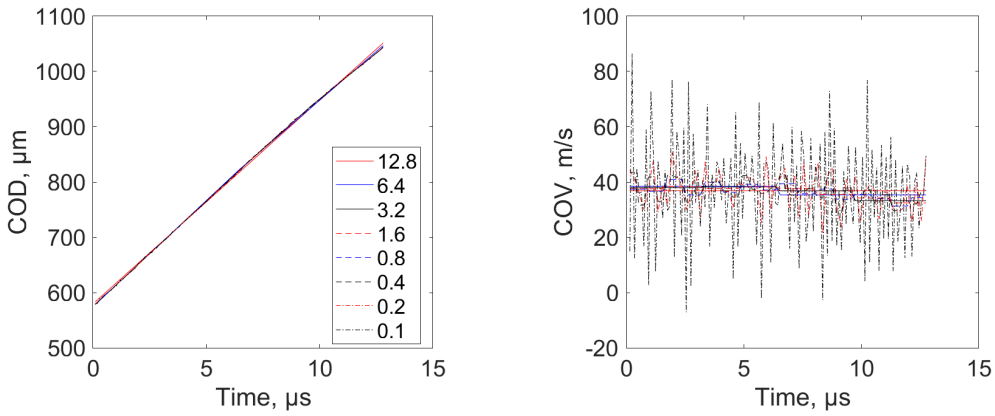

(a) (b)

Fig. 13. Mean crack opening displacement (a) and velocity (b) for different time discretizations

The major principal strain field is shown in Figure 14 for the last frame and different discretizations. These results are in line with displacement fields. This is to be expected since they were obtained by spatial differentiation only. Their levels being significantly higher than the corresponding uncertainties (Figure 7(c)), no significant difference is expected provided the captured kinematics was consistent with the experiment (Figure 11).

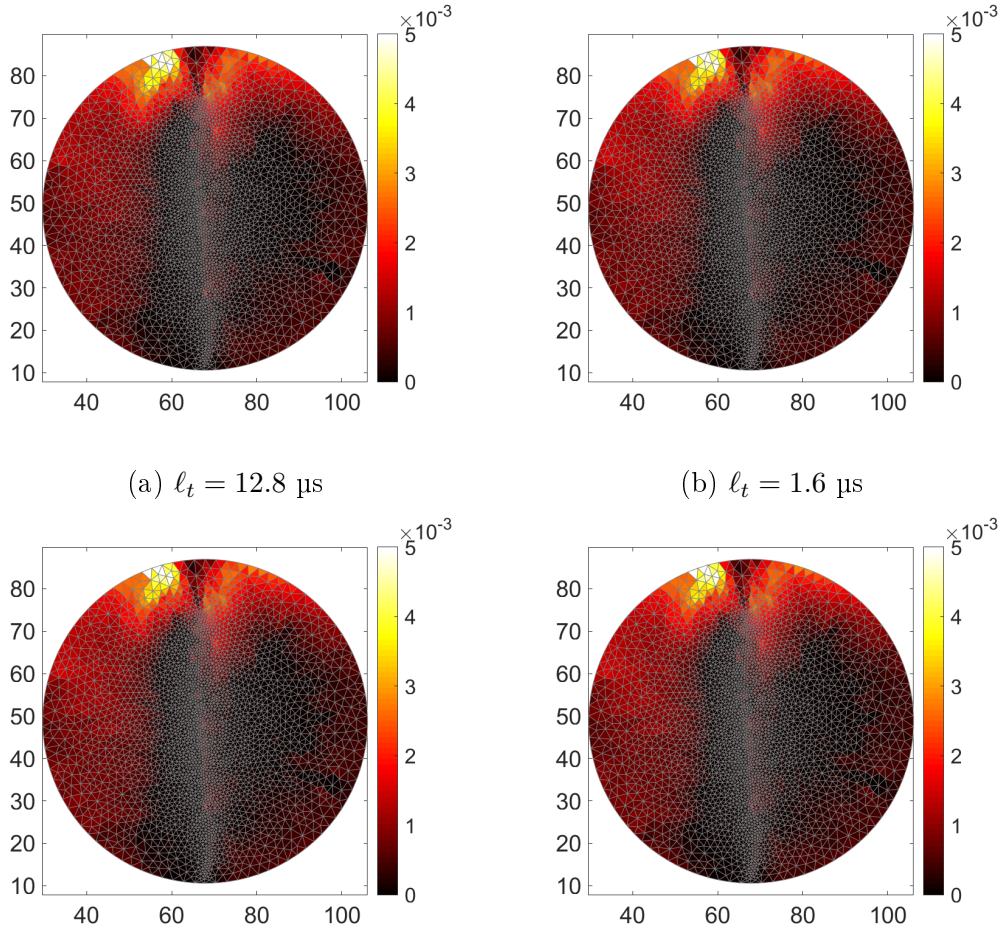

(a) $\ell_t = 12.8$ µs (b) $\ell_t = 1.6$ µs

(c) $\ell_t = 0.8$ µs (d) $\ell_t = 0.2$ µs

Fig. 14. Major principal strain field at the end of the video for different time discretizations

Contrary to the previous case, the major principal strain rate fields reported in Figure 15 are very different. This is due to the measurement uncertainties (Figure 7(d)). The effect of the temporal regularization is illustrated thanks to this last field. If consistent strain rates are sought, either spatiotemporal DIC is required or instantaneous DIC results would have to be filtered. Further, the strain rate field (Figure 15(a)) is consistent with the fact that rotations may be induced by the development of secondary cracks at the end of the video.

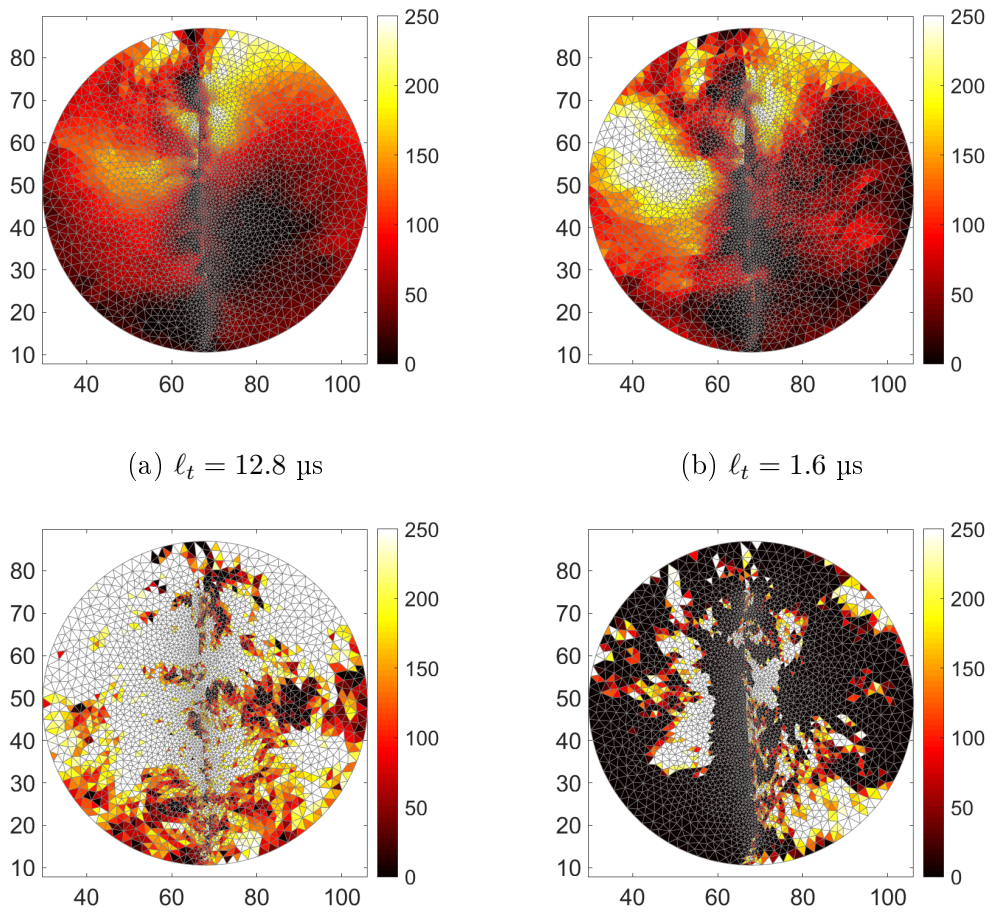

(a) $\ell_t = 12.8$ µs

(b) $\ell_t = 1.6$ µs

(c) $\ell_t = 0.8$ µs

(d) $\ell_t = 0.2$ µs

Fig. 15. Major principal strain rate field (expressed in 1/s) at the end of the video for different time discretizations

3.5 5 Mfps video

The acquisition rate was reduced to 5 Mfps to make triggering easier. The specimen remained motionless for about the first 50 frames. Then a complex multiple cracking pattern occurs (Figure 16). The cracks do not initiate simultaneously, namely, a first pair emanating from the bottom contact zone initiates after the 50th frame, while a third one between the first two appears at about the 120th frame. A fourth crack again vertical but located on the

right side emerges from the free surface.

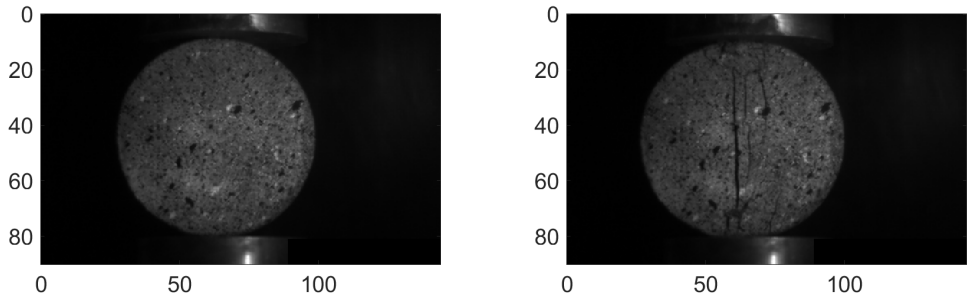

(a) (b)

Fig. 16. (a) Initial and (b) final frame of the 5 Mfps video. The dimensions are expressed in mm

As for the previous case, one of the major cracks was explicitly accounted for by following the above-described node splitting procedure. Given the temporal complexity of the cracking phenomena, it was expected that the temporal discretization would have a much more important effect. It was indeed observed that the mean gray level residuals depend on the discretization, namely, the smaller the time interval, the lower the overall residuals (Figure 17).

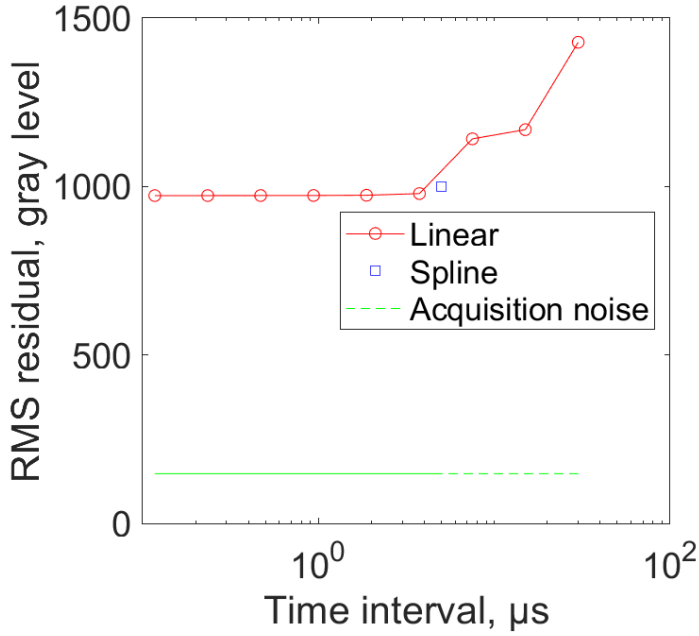

Fig. 17. RMS gray level residual for different time discretizations

This trend can be understood by analyzing the crack opening kinematics shown in Figure 18. A rather fine discretization was required in order to capture all the temporal details of the cracking phenomenon. This is particularly visible on the crack opening velocities (Figure 18(b)) that show different regimes and levels of velocities. However, with piece-wise linear interpolations, the acceleration fields cannot be estimated (without posterior smoothing process that was not performed herein). The measurement uncertainties are too high to provide any meaningful result (Figure 18(c)). Consequently, higher order interpolations are required.

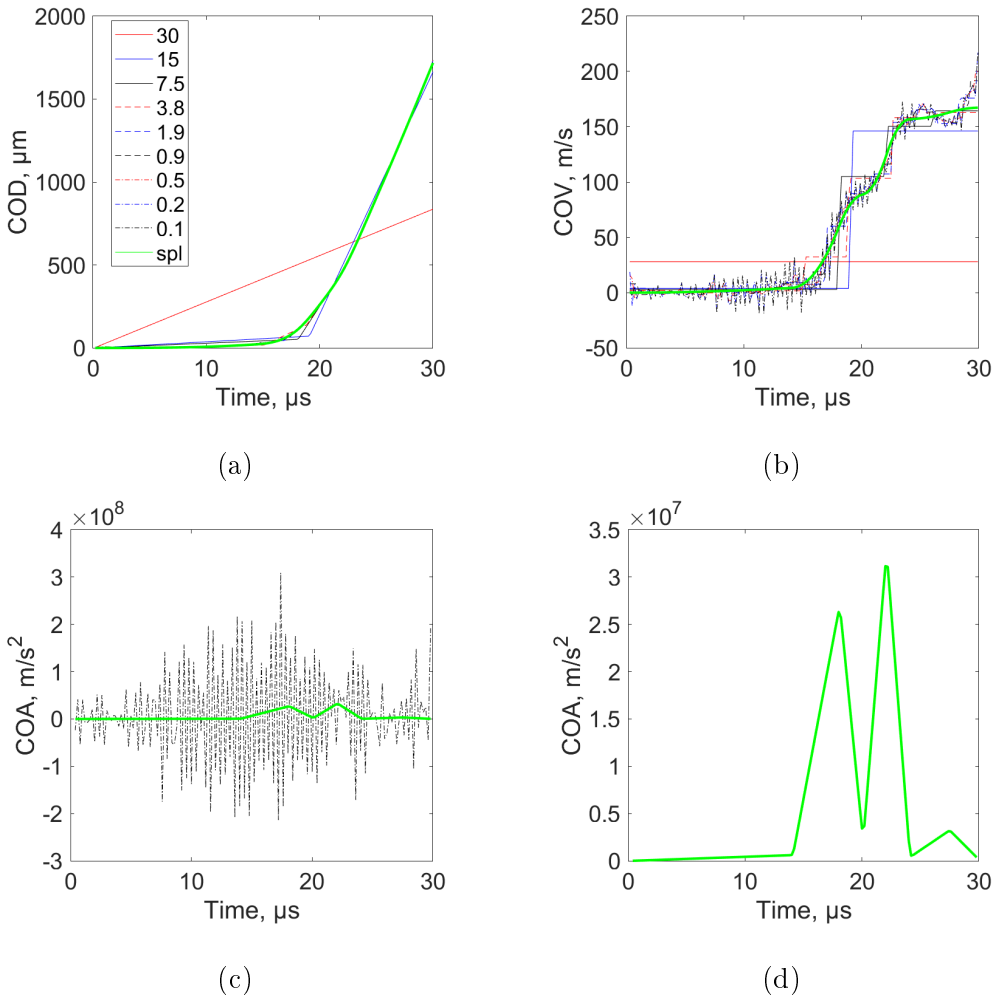

Fig. 18. Mean crack opening displacement (a), velocity (b), and acceleration (c) for different temporal discretizations. (d) Crack opening acceleration when a B-spline interpolation is considered

In the following, cubic B-spline interpolations were used. This choice allowed displacement and velocity fields to be continuous by construction. The continuity of the acceleration was also assumed during the whole analyzed sequence. Further, for the first temporal element the medium was assumed to be initially motionless (*i.e.,* the displacement, velocity and acceleration vanish at the initial time). For the last element, a natural spline was also implemented (*i.e.,* the acceleration was assumed to vanish at the last frame). Six elements

were considered. When all the previous conditions were accounted for, only 6 temporal degrees of freedom needed to be measured. With such parameterization, the gray level residuals were very close to those observed with a larger number of degrees of freedom (Figure 17). The crack opening displacements (Figure 18(a)), and more importantly crack opening velocities (Figure 18(b)) are in good agreement with the other discretizations except for the final time where the natural spline condition prescribes a constant velocity (which is probably not valid here). Further, the crack opening acceleration has a complex history (Figure 18(d)), which is consistent with the crack opening velocity history. Levels as high as 3×10^7 m/s^2 were reached.

Figure 19 compares two kinematic fields at the end of the video obtained via instantaneous DIC and when the B-spline interpolation is selected in the spacetime analyses. The displacement fields are very similar in both cases (Figure 19(a-b)). For the velocity fields, the differences are more pronounced (Figure 19(c-d)). Interestingly, spatial fluctuations appear in the velocity field measured via spacetime DIC. They are less resolved with instantaneous DIC. The acceleration fields, which correspond to the time for highest crack opening acceleration) are significantly different for both methods (Figure 19(e-f)). Only spacetime DIC provided acceleration fields that were meaningful (*i.e.,* their levels were significantly higher than the measurement uncertainties). The results of instantaneous DIC would have to be filtered to compute acceleration fields. Levels as high as $\pm 4 \times 10^7$ m/s^2 were reached in the reported field.

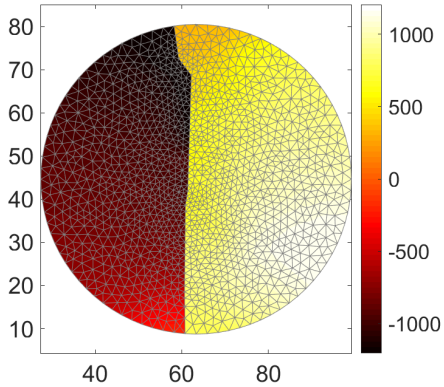

(a) $t = 30$ µs

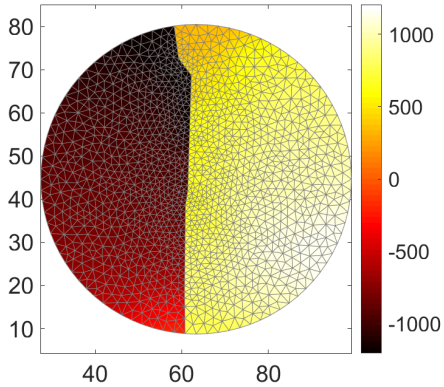

(b) $t = 30$ µs

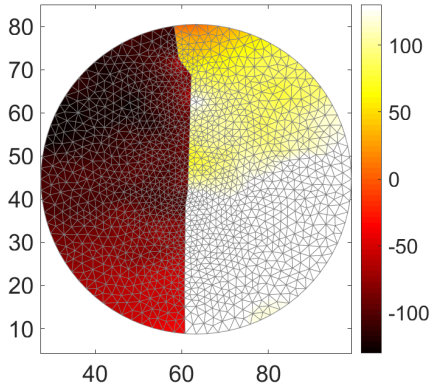

(c) $t = 30$ µs

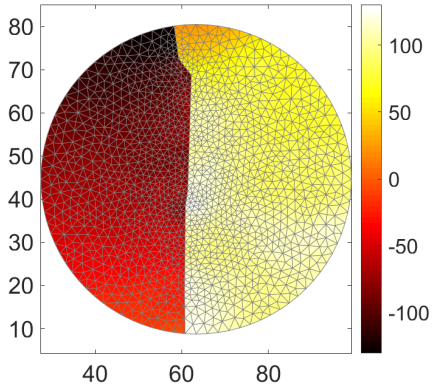

(d) $t = 30$ µs

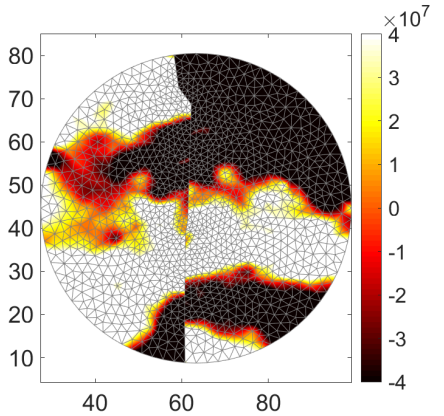

(e) $t = 24$ µs

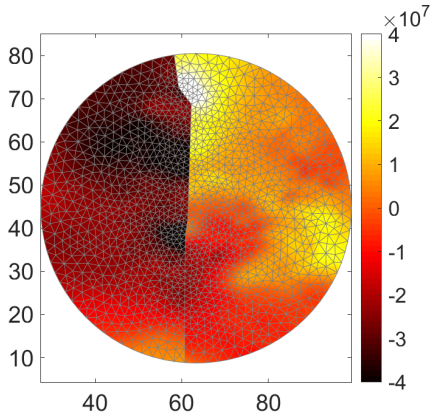

(f) $t = 24$ µs

Fig. 19. (a,b) Horizontal displacement fields (expressed in µm). (c,d) Horizontal velocity fields (expressed in m/s). (e,f) Horizontal acceleration fields (expressed in m/s^2). The left column corresponds to instantaneous DIC and the right column to spacetime DIC with B-spline interpolation

4 Conclusion

Digital image correlation was used to measure displacement, velocity, and acceleration fields via instantaneous and spacetime approaches of videos acquired with an ultra-high speed camera of two dynamic Brazilian tests. Major principal strains and strain rates were also evaluated with the previous technique. Maximum displacements of the order of 1 mm, velocities up to ± 200 m/s, and acceleration levels of ± 5 million g's were obtained. Similar levels were observed from the mean crack opening kinematics.

Uncertainty quantifications were performed with videos acquired prior to each experiment. With this information at hand, a denoised reference image could be constructed for each analyzed test. Further, the standard uncertainties were evaluated for the five kinematic quantities. With the selected camera, the acquisition noise was observed to be very small for 5 and 10 million frames per second videos. As a result, very low uncertainties were achieved even though ultra-high acquisition rates were used. Very significant gains were observed when spacetime discretizations could be used in comparison with standard (*i.e.,* instantaneous) analyses, especially for the acceleration fields.

It is worth noting that such uncertainty quantifications are very useful not only when analyzing impact tests as was illustrated herein but also for comparing or selecting a camera [5]. This approach is very generic and complies with the ASD-STAN prEN 4861 procedure for metrological assessment of kinematic fields measured by digital image correlation [48].

Acknowledgements

The authors wish to thank Dr. R. Akiki, Profs. F. Gatuingt, N. Schmitt and H. Zhao for fruitful discussions about the tests reported herein.

References

[1] D. Hopkinson, A method of measuring the pressure produced in the detonation of high explosives or by the impact of bullets, Phil. Trans. Roy. Soc. A 213 (1914) 437.

[2] H. Kolsky, An investigation of the mechanical properties of materials at very high rates of loading, Proc. Phys. Soc. London 62b (1949) 676–700.

[3] M. Sutton, J. Orteu, H. Schreier, Image correlation for shape, motion and deformation measurements: Basic Concepts, Theory and Applications, Springer, New York, NY (USA), 2009.

[4] J. Field, S. Walley, W. Proud, H. Goldrein, C. Siviour, Review of experimental techniques for high rate deformation and shock studies, Int. J. Impact Eng. 30 (2004) 725–775.

[5] F. Hild, A. Bouterf, P. Forquin, S. Roux, On the Use of Digital Image Correlation for the Analysis of the Dynamic Behavior of Materials, in: The Micro-World Observed by Ultra High-Speed Cameras, 2018, pp. 185–206.

[6] W. Peters, W. Ranson, Digital imaging techniques in experimental stress analysis, Opt. Eng. 21 (1982) 427–431.

[7] M. Sutton, W. Wolters, W. Peters, W. Ranson, S. McNeill, Determination of displacements using an improved digital correlation method, Im. Vis. Comp. 1 (3) (1983) 133–139.

[8] W. Peters, W. Ranson, J. Kalthoff, S. Winkler, A study of dynamic near-crack-tip fracture parameters by digital image analysis, J. Phys. Coll. 46 (C5) (1985) 631–638.

[9] Y. Chao, P. Luo, J. Kalthoff, An experimental study of the deformation fields around a propagating crack tip, Exp. Mech. 38 (2) (1998) 79–85.

[10] T. Etoh, Q. Nguyen, Evolution of High-Speed Image Sensors, Springer International Publishing, 2018, pp. 81–101.

[11] F. Barthelat, Z. Wu, B. Prorok, H. Espinosa, Dynamic torsion testing of nanocrystalline coatings using high-speed photography and digital image correlation, Exp. Mech. 43 (3) (2003) 331–340.

[12] J. Kajberg, M. Sjödahl, Optical method to study material behaviour at high strain rates, in: P. Ståhle, K. Sundin (Eds.), IUTAM Symposium on Field Analyses for Determination of Material Parameters – Experimental and Numerical Aspects, Vol. 109 of Solid Mechanics and its Applications, Springer (the Netherlands), 2003, pp. 37–49.

[13] A. Gilat, T. Schmidt, J. Tyson, Full field measurement during a tensile split hopkinson bar experiment, J. Phys. IV 134 (2006) 687–692.

[14] I. Elnasri, S. Pattofatto, H. Zhao, H. Tsitsiris, F. Hild, Y. Girard, Shock enhancement of cellular structures under impact loading: Part i experiments, J. Mech. Phys. Solids 55 (2007) 2652–2671.

[15] J. Kajberg, B. Wikman, Viscoplastic parameter estimation by high strain-rate experiments and inverse modelling – speckle measurements and high-speed photography, Int. J. Solids Struct. 44 (1) (2007) 145–164.

[16] P. Reu, T. Miller, The application of high-speed digital image correlation, J. Strain Anal. 43 (8) (2008) 673–688.

[17] V. Tarigopula, O. Hopperstad, M. Langseth, A. Clausen, F. Hild, A study of localisation in dual phase high-strength steels under dynamic loading using digital image correlation and fe analysis, Int. J. Solids Struct. 45 (2) (2008) 601–619.

[18] F. Pierron, M. Sutton, V. Tiwari, Ultra high speed dic and virtual fields method analysis of a three point bending impact test on an aluminium bar, Exp. Mech. 51 (4) (2011) 537–563.

[19] D. Saletti, S. Pattofatto, H. Zhao, Measurement of phase transformation properties under moderate impact tensile loading in a niti alloy, Mech. Mat. 65 (2013) 1–11.

[20] Search with PUBLICATION NAME: (international journal of impact engineering) & TOPIC: (image correlation), [accessed September 5, 2018], www.webofknowledge.com.

[21] V. Tiwari, M. Sutton, S. McNeill, S. Xu, X. Deng, W. Fourney, D. Bretall, Application of 3d image correlation for full-field transient plate deformation measurements during blast loading, International Journal of Impact Engineering 36 (6) (2009) 862–874.

[22] D. Dubois, H. Zellmer, E. Markiewicz, Experimental and numerical analysis of seat belt bunching phenomenon, International Journal of Impact Engineering 36 (6) (2009) 763–774.

[23] P. Hogström, J. Ringsberg, E. Johnson, An experimental and numerical study of the effects of length scale and strain state on the necking and fracture behaviours in sheet metals, International Journal of Impact Engineering 36 (10) (2009) 1194–1203.

[24] F. Lauro, B. Bennani, D. Morin, A. Epee, The SEĖ-method for determination of behaviour laws for strain rate dependent material: Application to polymer material, International Journal of Impact Engineering 37 (6) (2010) 715–722.

[25] R. Moura, A. Clausen, E. Fagerholt, M. Alves, M. Langseth, Impact on hdpe and pvc plates - experimental tests and numerical simulations, International Journal of Impact Engineering 37 (6) (2010) 580–598.

[26] J. Peirs, P. Verleysen, W. V. Paepegem, J. Degrieck, Determining the stress-strain behaviour at large strains from high strain rate tensile and shear experiments, International Journal of Impact Engineering 38 (5) (2011) 406–415.

[27] A. Collins, J. Addiss, S. Walley, K. Promratana, F. Bobaru, W. Proud, D. Williamson, The effect of rod nose shape on the internal flow fields during the ballistic penetration of sand, International Journal of Impact Engineering 38 (12) (2011) 951–963.

[28] J. LeBlanc, A. Shukla, Response of e-glass/vinyl ester composite panels to underwater explosive loading: Effects of laminate modifications, International Journal of Impact Engineering 38 (10) (2011) 796–803.

[29] P. Kumar, J. LeBlanc, D. Stargel, A. Shukla, Effect of plate curvature on blast response of aluminum panels, International Journal of Impact Engineering 46 (2012) 74–85.

[30] G. Besnard, F. Hild, J. Lagrange, P. Martinuzzi, S. Roux, Analysis of necking in high speed experiments by stereocorrelation, Int. J. Impact Eng. 49 (2012) 179–191.

[31] K. Spranghers, I. Vasilakos, D. Lecompte, H. Sol, J. Vantomme, Numerical simulation and experimental validation of the dynamic response of aluminum plates under free air explosions, International Journal of Impact Engineering 54 (2013) 83–95.

[32] R. Ambriz, C. Froustey, G. Mesmacque, Determination of the tensile behavior at middle strain rate of aa6061-t6 aluminum alloy welds, International Journal of Impact Engineering 60 (2013) 107–119.

[33] J. Seidt, J. Pereira, A. Gilat, D. Revilock, K.Nandwana, Ballistic impact of anisotropic 2024 aluminum sheet and plate, International Journal of Impact Engineering 62 (2013) 27–34.

[34] L. Wang, Y. Ding, L. Yang, Experimental investigation on dynamic constitutive behavior of aluminum foams by new inverse methods from wave propagation measurements, International Journal of Impact Engineering 62 (2013) 48–59.

[35] M. O'Masta, B. Compton, E. Gamble, F. Zok, V. Deshpande, H. Wadley, Ballistic impact response of an uhmwpe fiber reinforced laminate encasing of an aluminum-alumina hybrid panel, International Journal of Impact Engineering 86 (2015) 131–144.

[36] M. Louar, B. Belkassem, H. Ousji, K. Spranghers, D. Kakogiannis, L. Pyl, J. Vantomme, Explosive driven shock tube loading of aluminium plates: experimental study, International Journal of Impact Engineering 86 (2015) 111–123.

[37] G. Gruben, M. Langseth, E. Fagerholt, O. Hopperstad, Low-velocity impact on high-strength steel sheets: An experimental and numerical study, International Journal of Impact Engineering 88 (2016) 153–171.

[38] B. Koohbor, A. Kidane, W.-Y. Lu, M. Sutton, Investigation of the dynamic stress-strain response of compressible polymeric foam using a non-parametric analysis, International Journal of Impact Engineering 91 (2016) 170–182.

[39] M. Omidvar, M. Iskander, S. Bless, Soil-projectile interactions during low velocity penetration, International Journal of Impact Engineering 93 (2016) 211–221.

[40] B. Koohbor, A. Kidane, M. Sutton, X. Zhao, S. Mallon, Analysis of dynamic bending test using ultra high speed dic and the virtual fields method, International Journal of Impact Engineering 110 (2017) 299–310.

[41] H. Xing, Q. Zhang, D. Ruan, S. Dehkhoda, G. Lu, J. Zhao, Full-field measurement and fracture characterisations of rocks under dynamic loads using high-speed three-dimensional digital image correlation, International Journal of Impact Engineering 113 (2018) 61–72.

[42] G. Broggiato, L. Casarotto, Z. Del Prete, D. Maccarrone, Full-field strain rate measurement by white-light speckle image correlation, Strain 45 (4) (2009) 364–372.

[43] G. Besnard, S. Guérard, S. Roux, F. Hild, A space-time approach in digital image correlation: Movie-DIC, Optics Lasers Eng. 49 (2011) 71–81.

[44] G. Besnard, H. Leclerc, S. Roux, F. Hild, Analysis of image series through digital image correlation, J. Strain Analysis 47 (4) (2012) 214–228.

[45] M. Berny, T. Archer, A. Mavel, P. Beauchêne, S. Roux, F. Hild, On the analysis of heat haze effects with spacetime DIC, Opt. Lasers Eng. 40 (2018) 544–556.

[46] G. Besnard, F. Hild, S. Roux, "Finite-element" displacement fields analysis from digital images: Application to Portevin-Le Chatelier bands, Exp. Mech. 46 (2006) 789–803.

[47] F. Hild, S. Roux, Comparison of local and global approaches to digital image correlation, Exp. Mech. 52 (9) (2012) 1503–1519.

[48] ASD-STAN prEN 4861 P1 Aerospace series-Metrological assessment procedure for kinematic fields measured by digital image correlation, [accessed September 5, 2018], www.asd-stan.org/downloads/asd-stan-pren-4861-p1/.

[49] M. Berny, C. Jailin, A. Bouterf, F. Hild, S. Roux, Model Reduction for Space-Time DIC, Mea. Sci. Technol. 29 (12) (2018) 125008.

[50] ISO, Guide to the Expression of Uncertainty in Measurements (GUM), International Organization for Standardization, Geneva (Switzerland), 1995.

[51] F. Lobo Carneiro, Um novo método para determinacão da resistência à tração dos concretos, in: Anais 5a reunião da Associação Brasileira de Normas Técnicas (ABNT) em São Paulo, 1943, pp. 127–129.

[52] F. Lobo Carneiro, Une nouvelle méthode pour la détermination de la résistance à la traction des bétons, Bull. RILEM 13 (1953) 103–108.

[53] Z. Tomičević, F. Hild, S. Roux, Mechanics-aided digital image correlation, J. Strain Analysis 48 (2013) 330–343.